RSC Advances

PAPER

View Article Online
View Journal | View Issue

Cite this: *RSC Adv.*, 2025, **15**, 655

Unlocking advanced thermometric capabilities: $BiVO_4$: Er^{3+}/Yb^{3+} nanophosphors with dual-mode up-conversion and down-shifting features

Fadwa Ayachi,[a] Kamel Saidi,[a] Mohamed Dammak, *[a] Irene Mediavilla[b] and Juan Jiménez[b]

Luminescent materials doped with rare-earth (RE) ions have emerged as powerful tools in thermometry, offering high sensitivity and accuracy. However, challenges remain, particularly in maintaining efficient luminescence at elevated temperatures. This study investigates the thermometric properties of $BiVO_4$: Yb^{3+}/Er^{3+} (BVO: Er/Yb) nanophosphors synthesized *via* the sol–gel method. Structural, morphological, and optical analyses confirm the high purity and monoclinic crystal structure of the materials. Dual-mode luminescence under UV and near-infrared (NIR) excitation is explored, revealing complex thermal dynamics. The distinct performances of these luminescent thermometers, in terms of thermal sensitivity and temperature uncertainty, were evaluated in the non-saturation regime in both down-shifting (DS) and up-conversion (UC) processes. Utilizing fluorescence intensity ratio (LIR) measurements, we quantified absolute and relative sensitivities, as well as temperature uncertainties, over a temperature range of 300–450 K. Temperature sensing was based on the LIR of green emission bands arising from the thermally coupled $^2H_{11/2} \rightarrow {}^4I_{15/2}$ and $^4S_{3/2} \rightarrow {}^4I_{15/2}$ transitions of Er^{3+}. The maximum absolute sensitivity (S_a) reached 60×10^{-4} K^{-1} at 388 K under 975 nm excitation (UC) and 56×10^{-4} K^{-1} at 400 K under 325 nm excitation (DS). Notably, for both excitation modes, the relative sensitivity (S_r) decreased consistently with increasing temperature, peaking at 0.908% K^{-1} and 0.87% K^{-1} at 300 K, and gradually declining to 0.4% K^{-1} and 0.39% K^{-1} at 450 K for the DS and UC processes, respectively. Temperature resolution (δT) also varied with temperature, increasing from 0.55 K to 1.23 K as the temperature rose from 300 to 450 K under 325 nm excitation. A comparable trend was observed for δT under 975 nm excitation. These findings underscore the potential of BVO: Er/Yb nanophosphors as versatile and effective luminescent thermometers for a broad range of applications.

Received 5th December 2024
Accepted 27th December 2024

DOI: 10.1039/d4ra08590f

rsc.li/rsc-advances

1. Introduction

In recent years, there has been a surge in interest in the development and exploration of new phosphor materials due to their diverse applications in display devices, solar cells, temperature sensors, bioimaging, and more. These materials possess the remarkable ability to convert short-wavelength light into longer-wavelength light, including the ability to convert absorbed higher-energy photons into two lower-energy photons, known as the down-shifting (DS) process when an appropriate mix of Ln^{3+} dopants is selected.[1–5] Conversely, the reverse process, known as up-conversion (UC), is also achievable, wherein two or more photons in the IR or NIR range may be converted to photons of higher energy. Materials that exhibit both DS and UC properties, termed dual-mode luminescence, are particularly intriguing yet exceedingly rare.

Luminescent thermometers, primarily based on spectroscopic parameters, have garnered significant attention due to their excellent accuracy, high sensitivity, and rapid response. The LIR thermometry method is recognized as a promising approach for optical temperature measurement as compared to other optical temperature sensing techniques, owing to its independence from external factors, such as spectral loss and fluctuations in excitation power.[6–9] The LIR technique has demonstrated remarkable anti-interference capabilities and enhanced sensitivity, particularly in temperature measurements in electromagnetic and adverse environments, such as building fire detection, micro/nano-scale detection, and biomedical imaging systems.[10–14] Typically, the LIR technique relies on the luminescence emission from thermally coupled levels (TCL) of RE, which holds significant potential, especially in challenging environments like oil refineries and coal mines.[15–17] Much of the research has focused on Er^{3+}-activated detection materials, which can exhibit intense luminescence,

---

[a] Département de Physique, Laboratoire de Physique Appliquée, Faculté des Sciences de Sfax, Université de Sfax, BP 1171 Sfax, Tunisia. E-mail: madidammak@yahoo.fr; Mohamed.dammak@fss.usf.tn

[b] Department of Condensed Matter Physics, GdS Optronlab, LUCIA Building, University of Valladolid, Paseo de Belén 19, 47011, Valladolid, Spain

especially with the assistance of Yb^{3+} sensitizers.[18–21] Optical temperature sensing is commonly achieved through the green emissions of suitable TCLs, such as $^2H_{11/2}$ and $^4S_{3/2}$ in Er^{3+}.[22,23] Understanding the variation in LIR with temperature is crucial for practical detection applications.

The effectiveness of up-conversion emission intensity in optical thermometry hinges significantly on the host material's characteristics. Glasses and fluorides, commonly used for temperature sensors, exhibit substantial emission signals even under low excitation power.[24–27] However, their limited stability impedes widespread commercialization, with glasses additionally restricted by their transition temperature.[28] Composite materials incorporating nanocrystals in glass-ceramics offer improved stability but suffer from reduced thermal sensitivity.[29,30] $BiVO_4$ host presents a promising solution due to their efficient NIR to visible up conversion properties,[31,32] and excellent stability even at temperatures up to 800 °C.

Indeed, $BiVO_4$ is a low-symmetry host with a highly asymmetric crystal field surrounding the dopant.[33] This crystal field facilitates efficient 4f–f transitions in Ln^{3+} dopant ions, thus enhancing the up-conversion emission. The layered structure of $BiVO_4$ contains cations with formal oxidation states of Bi^{3+} ($6s^2$) and V^{5+} ($3d^0$) coordinated with O^{-2} ($2p^6$), alongside with a slight crystal structure distortion.[34] These characteristics not only promote weak hole-localization and electron–hole pair separation but also contribute to high up conversion emission efficiencies. $BiVO_4$ meets these criteria with moderately low phonon energy, minimizing non-radiative losses, and maximizing radiative emission. Thus, $BiVO_4$ shows promise as a potential up conversion host material.[32,35,36] This material has already been explored for luminescence thermometry with promising performance improvements.[37–39] However, the effects of excitation on the up conversion (UC) and down shifting (DS) processes have not yet been investigated. In this study, Er^{3+}/Yb^{3+} codoped $BiVO_4$ phosphors were prepared *via* a sol–gel method. We investigated the optical temperature sensing properties through up-conversion (UC) and down-shifting (DS) processes. Comparisons were made regarding the performance of BVO: Er/Yb nanophosphors in luminescence thermometric applications under DS (325 nm) and UC (975 nm) excitations.

2. Synthesis and characterization

The sol gel method was used to prepare pure and Yb/Er codoped $BiVO_4$ powders, in which Er_2O_3 (99.99%), Yb_2O_3 (99.99%) and analytical grade reagents (A.R.): ammonium metavanadate (NH_4VO_3), nitric acid (HNO_3), citric acid, bismuth nitrate [$Bi(NO_3)_3$–$9H_2O$], were served as the raw materials with mole ratio of 1 : 1 in ethanol at 70 °C for 1 hour. The obtained sol was changed to the yellow gel after addition of deionized water and acetic acid. The yellow gel was dried at 100 °C for 48 h and calcined at 400–600 °C for 2 h. The phase purity of $BiVO_4$ powder was studied by X-ray diffraction (XRD). The morphology of $BiVO_4$ powder was investigated by scanning electron microscopy (SEM) using a Scanning Electron Microscope FEI Quanta 250 FEG. Absorption spectra were collected using a Lambda 365 UV-vis spectrometer (PerkinElmer) in the 200–1100 nm range. The UC photoluminescence (PL) spectra were measured by using a 975 nm InGaAs/GaAs laser diode as the excitation source, with the HORIBA Jobin Yvon Fluorolog-3 Spectrofluorometer system. The Raman spectra and the DS photoluminescence (PL) spectra were recorded under excitation with a He–Cd laser (325 nm) with a Labram UV-HR 800 Raman spectrometer from Horiba-Jobin Yvon using a low dispersion 150 g mm^{-1} grating. Through 325 nm and 975 nm diode laser excitations at constant pump power of 30 mW the emission spectra were recorded on monochromator (Horiba Jobin Yvon, iHR320) spectrometer. The monochromator uses an 1800 g per mm grating blazed at 500 nm and a photomultiplier tube (Hamamatsu, R928) to measure luminescence in the green (520–570 nm) emission bands. The chemicals and equipment were procured from suppliers through the facilities at the University of Valladolid, Spain, and the University of Sfax, Tunisia.

3. Results and discussions

3.1. X-ray diffraction and morphological analysis

The X-ray diffraction (XRD) pattern was registered using a Bruker AXS D8 Advance diffractometer in Bragg–Brentano geometry (2θ range from 20° to 80°) with $CuK\alpha_1$ radiation (λ = 1.5406 Å). The XRD patterns of samples BVO and BVO: Yb/Er display sharp diffraction peaks as depicted in Fig. 1, which indicates the high crystallinity of these samples. The diffraction peaks of the BVO and BVO: Yb/Er samples agree well with the monoclinic structure of BVO (JCPDS#96-901-3438). This monoclinic host structure provides a highly asymmetric crystal field around the Ln^{3+} ions, which should favor the 4f → 4f transitions. Moreover, the diffraction peak of the Ln^{3+} doped sample moves to a higher angle direction compared to the standard card (JCPDS#96-901-3438).[40,41] This shift is caused by the substitution of Bi^{3+} (ionic radius1.03 Å) with Yb^{3+} (0.858 Å) and Er^{3+} (1.004 Å) doped ions. Thus, revealing the successful incorporation of Yb^{3+} and Er^{3+} into the $BiVO_4$. The surface morphology of the particles in the prepared BVO undoped and doped Er/Yb were studied with SEM micrographs and presented in Fig. 2(a) and (b) respectively. A spherical structure is observed, and the particles have uniform shapes and regular sizes. The average size of particles is about 1 μm.

3.2. Raman studies

Fig. 3 displays the Raman spectra of BVO pure and doped with Er^{3+}/Yb^{3+} excited with 532 nm (doubled YAG laser) at a resolution of 2 cm^{-1} in the range 150–1400 cm^{-1}. We can clearly see that the two spectra are similar, confirming the absence of structural changes by an incorporation of Er^{3+}/Yb^{3+} into the host BVO. The peak at 828 cm^{-1} is assigned to the V–O symmetric stretching vibration (υ_s),[42] whereas the peak at 366 cm^{-1} is attributed to the bending vibration of the VO_4^{-3} group (δ).[43] The peak at 329 cm^{-1} corresponds to the symmetric V–O bending mode. Other bands peaking at 213 cm^{-1} and 127 cm^{-1} are combined with external modes of the VO_4^{-3}

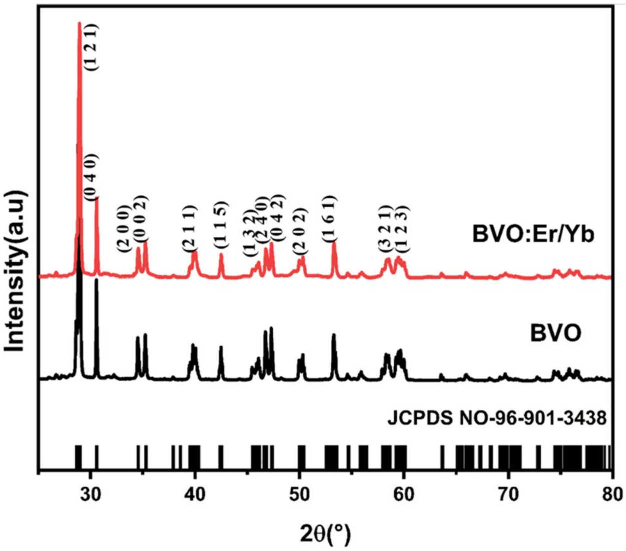

Fig. 1 XRD patterns of pure BVO and BVO: Er/Yb samples. The corresponding standard JCPDS card data of BVO (JCPDS##96-901-3438) is given as a reference.

group.[44] These Raman peaks are the typical vibrational bands of BVO.

3.3. UV-visible spectroscopy

Fig. 4(a) display the UV-vis-NIR diffuse reflectance spectra of pure BVO as well as Yb^{3+}/Er^{3+} codoped BVO samples. There are two sharp absorption bands seen in both the undoped and Yb^{3+}/Er^{3+} doped samples at 260 and 314 nm which are due to the charge transfer band (CTB) between V^{5+} and O^{2-}. These strong absorption bands in the UV window are caused by the Vanadate $(VO_4)^{3-}$ group which acts as a self-activating host.[45] In addition to these broad CTB bands, there are also a few peaks observed in the Er^{3+}/Yb^{3+} codoped samples at 649 and 720 nm due to transitions from the $^4I_{15/2}$ ground state to different excited states, namely $^4F_{9/2}$ and $^4I_{9/2}$ of the Er^{3+} ions, respectively, as shown in Fig. 4. The absorption peaks around 980 nm of the BVO: Er/Yb sample is assigned to the $^2F_{7/2} \rightarrow {}^2F_{5/2}$ transition of the Yb^{3+} ion.

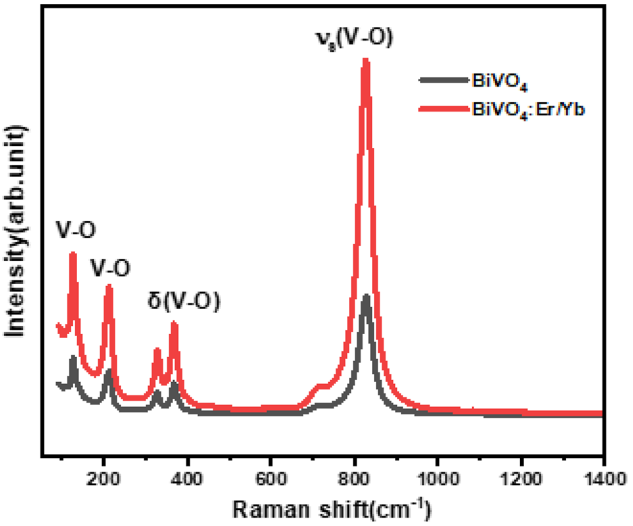

Fig. 3 Raman spectra of pure BVO and BVO: Er/Yb samples.

The sharp absorption intensity observed at 980 nm is indicative of the strong absorption cross-section of Yb^{3+} ions in this spectral region. The doping concentration of Yb^{3+} ions play

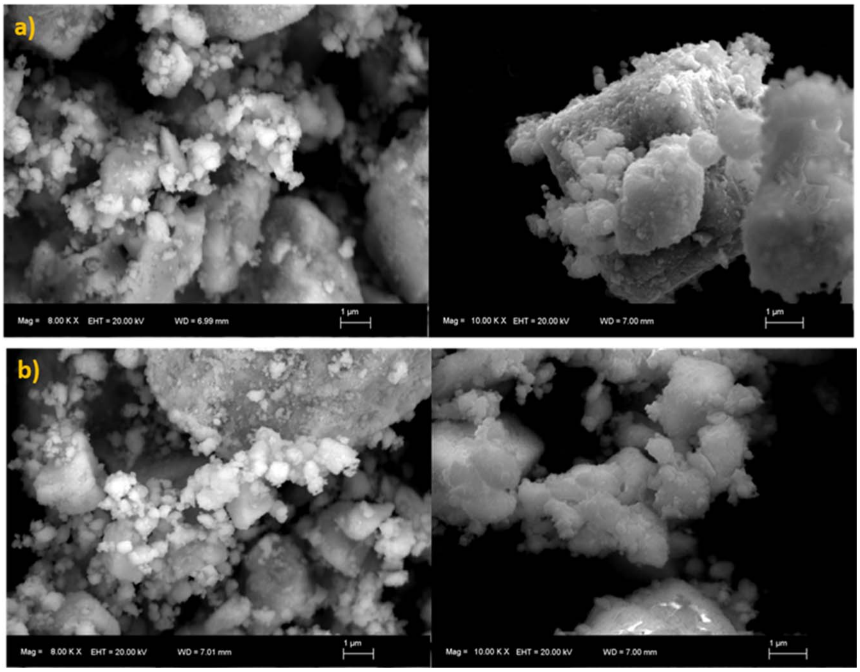

Fig. 2 (a) and (b) The SEM images of the BVO pure and BVO doped Er/Yb samples, respectively.

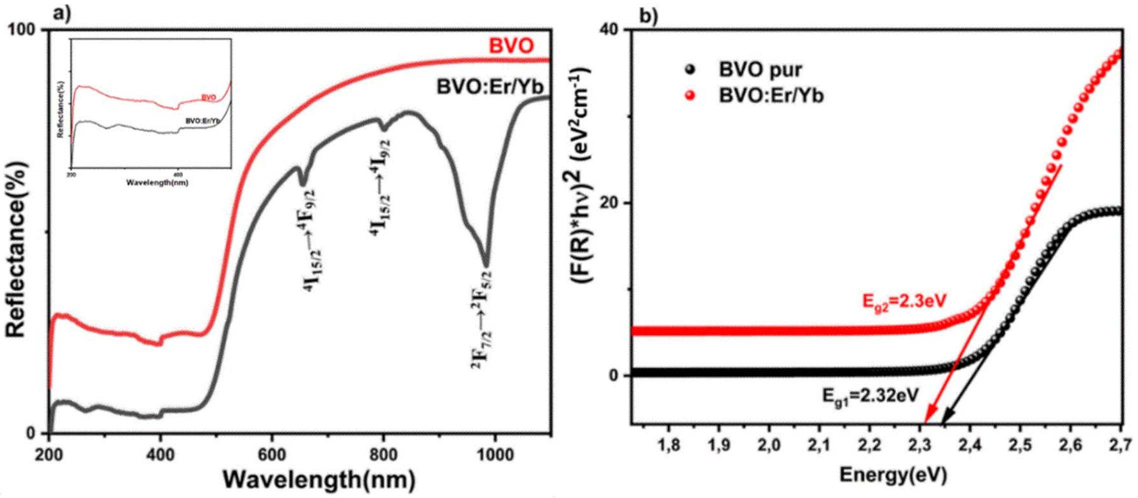

Fig. 4 (a) UV-vis-NIR diffuse reflectance spectra (inset spectra from 200–500 nm region), (b) the plot of gap energy of pure BVO and BVO: Er/Yb samples.

a critical role in determining the intensity and sharpness of this absorption feature. At lower doping concentrations, the 980 nm absorption peak remains sharp and well-defined due to minimal ion–ion interactions. However, at higher doping levels, enhanced ion interactions can lead to a broadening or slight diminution in sharpness, altering the spectroscopic behavior. This concentration-dependent variation underscores the importance of optimizing Yb^{3+} ion doping for specific applications. In addition, the Kubelka–Munk function can be applied to determine the band gap size which can be expressed as follows eqn (1):

$$((F(R)h\vartheta)^n) = B(h\vartheta - E_g) \quad (1)$$

where hv is the incident photon energy, C is a constant of proportionality and E_g is the band gap (eV). Fig. 4(b) shows the evolution of $(F(R)hv)^2$ as a function of hv. The E_g values are estimated as 2.32 eV and 2.3 eV for BVO pure and BVO: Yb^{3+}/Er^{3+}, respectively. This large band gap of the host effectively accommodates the energy levels of the dopant ions to produce luminescence.

4. UC and DS luminescent properties of NPs

Fig. 5(a) and (b) represent the PL spectra of BVO: Er^{3+}/Yb^{3+} phosphor excited with UV (325 nm) and IR (975 nm). Sensitizer ion concentrations commonly utilized exceed 15 mol% (Yb^{3+}) to produce a strong UC emission, whereas emitter ion concentrations of about 2% work well based on our previous work.[46] The DS and UC emission spectra exhibit two strong emission bands linked to the $^2H_{11/2}$/$^4I_{15/2}$ (525 nm) and $^4S_{3/2}$/$^4I_{15/2}$ (552 nm) transitions of Er^{3+} ions. The emission intensity of the BVO phosphor under DS luminescence is much higher than under up conversion luminescence. This indicates that host material

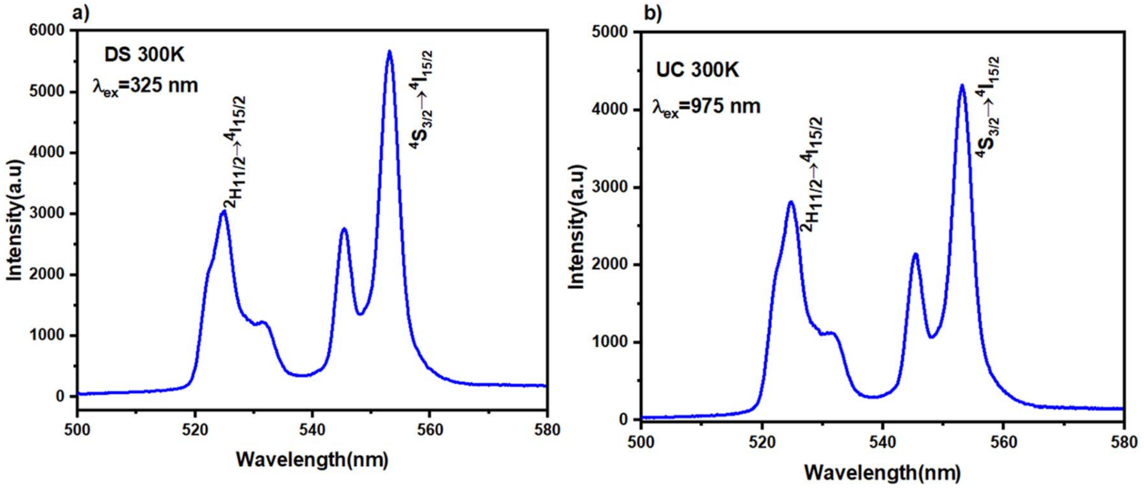

Fig. 5 Emission spectra of BVO: Er/Yb at room temperature (a) under 325 nm excitation (DS), (b) under 975 nm excitation (UC), respectively.

has some impact on the UC and DS luminescence. Analogous outcomes were reported in other studies carried out in diverse phosphors, which were ascribed to a mechanism of borrowing intensity that blends the 4f and 5d RE orbits through the valence band energy levels of the lattice.[46–50]

Substantial evidence suggests that high excitation density can lead to the saturation of intermediate up-converting levels, resulting in a reduction of photon absorption by the ground state due to its carrier depletion. Consequently, it can readily saturate the anti-Stokes emission conversion. The importance of excitation pump power in luminescence thermometry was underscored by previous research, indicating that achieving high sensitivity necessitates excitation in the non-saturation regime.

In the subsequent phase of our research, we will utilize a minimum excitation pump power of 30 mW to activate the up-conversion mechanism in BVO: Er/Yb. Accordingly, for future thermometric inquiries, we will maintain a constant 30 mW excitation for both the UC and DS processes.

Such spectral properties will be beneficial to obtain a reliable temperature sensing behavior of BVO: Er/Yb phosphor. For the UC process, the UC emission intensity (I) depends on the pump power (P) eqn (2):[51–53]

$$I \propto P^n \tag{2}$$

wherein n is roughly equal to the number of pump photons necessary to excite the RE ions from ground state to the excited state at relatively small pump power. n can be estimated from an exponential fit of the intensity *versus* pump power plot using eqn (2). Fig. 6 presents the linear fit slopes (n) for the green emission associated with $^2H_{11/2}$ and $^4S_{3/2}$ upon 975 nm excitation, they are estimated separately to be 1.8 and 1.65, respectively. This suggest that the populations of these states are ($^2H_{11/2}$, $^4S_{3/2}$, $^4F_{9/2}$) are mainly contributed by two-photon absorption process.[54–56] Based on the previous results, a scheme for the luminescence processes under NIR and UV excitation can be drawn. Fig. 7 illustrates the diagrams of the energy levels of Er^{3+} and Yb^{3+} ions and the tentative diagrams of the DS and UC processes. Here, we set up possible excitation and emission transitions, and energy transfer path between sensitizer (Yb^{3+}) and activator (Er^{3+}) in BVO. These processes have been widely discussed in the literature. The different radiative and non-radiative pathways implicated in the PL scheme of BVO are represented in the energy level plot of Fig. 7. Upon excitation with 325 nm (DS), vanadate ion in the ground state $^1A_1$ can be promoted to the $^1T_2$ state, then relaxes non-radiatively to the $^1T_1$ state. The excited state energy level $^1T_1$ of vanadate is almost aligned with the $^4G_{11/2}$ Er^{3+} excitable state, leading to a non-radiative resonance energy transfer from the vanadate to Er^{3+} ions. The $^4G_{7/2}$ excited state of Er^{3+} is non-radiatively depleted to the $^2H_{11/2}$ and $^4S_{3/2}$ emitting states of Er^{3+} ions, which result in the green emission at 525 and 547 nm, respectively, which permits to explain the DS mechanism.[57,58] Upon excitation through 975 nm (UC), first, the Yb^{3+} ion absorbs NIR photons at 975 nm promoting it to its excited state. Second, energy transfer from Yb^{3+} to Er^{3+} ions take place, exciting Er^{3+} to the $^4I_{11/2}$ state and then to the $^4F_{7/2}$ state. Third, the Er^{3+} ion in the $^4F_{7/2}$ state relaxes quickly to the lower energy $^2H_{11/2}$/$^4S_{3/2}$ states. Finally, the $^2H_{11/2}$/$^4S_{3/2}$–$^4I_{15/2}$ transitions take place, producing the green emission.

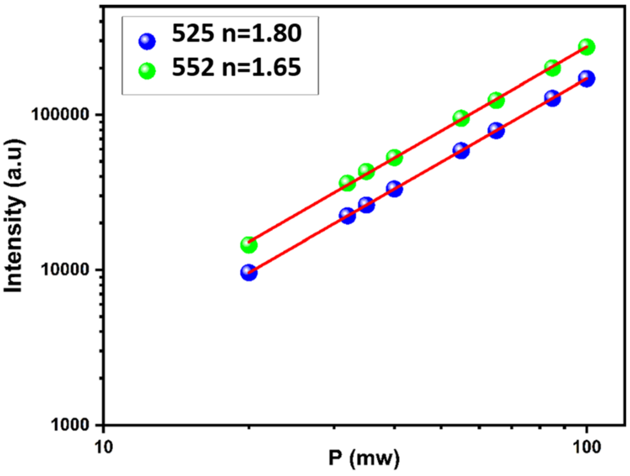

Fig. 6 Integral emission intensity of the green and red emission lines as a function of the pump laser power (975 nm excitation).

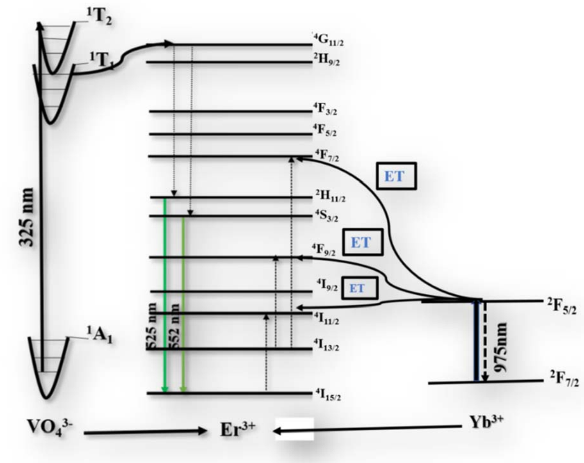

Fig. 7 Schematic energy level diagram of Er^{3+} and Yb^{3+} ions and mechanisms.

5. Temperature sensing behavior

To evaluate the potential application of Yb^{3+}/Er^{3+} codoped BVO phosphor in dual-mode optical thermometry, the temperature-dependent luminescence behavior of the samples was studied in detail under both 325 nm and 975 nm excitations.

Fig. 8 depicts the temperature-dependent emission spectra in the range of 400–700 nm of the phosphor BVO: Er/Yb excited under 325 nm and 975 nm respectively. For both UC and DS, all the spectra produced by the investigated phosphor exhibit two peaks ascribed to the Er^{3+} ion transitions and they are located in the green (G) visible region, namely, 525 nm: $^2H_{11/2} \rightarrow {}^4I_{15/2}$ and

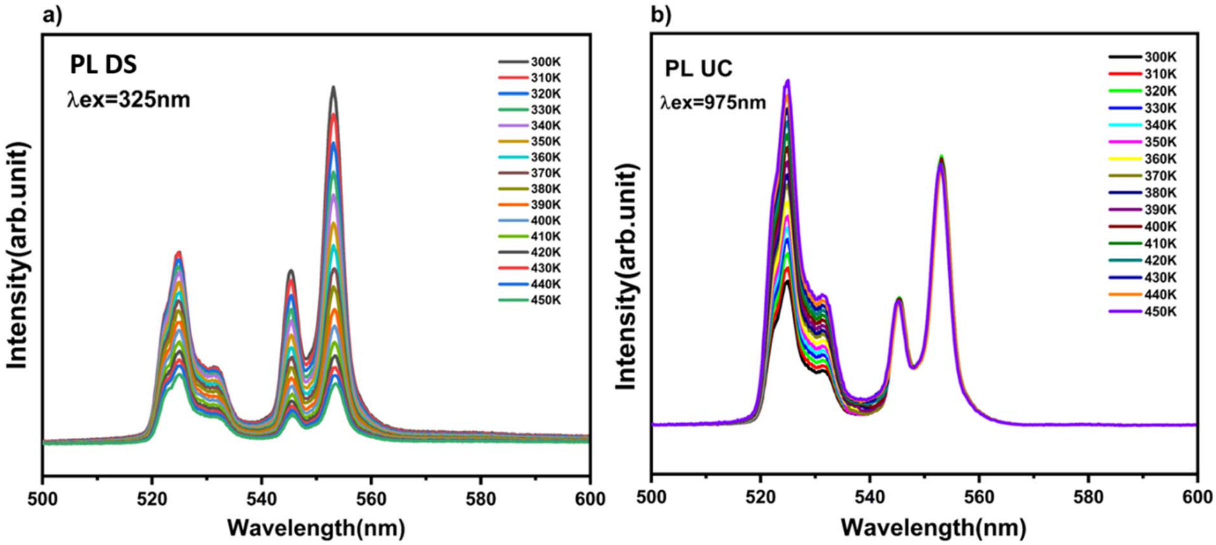

Fig. 8 Emission spectra of the BVO: Yb/Er phosphor for different temperatures in the visible range (a) under 325 nm excitation (DS), (b) under 975 nm (UC) excitation.

552 nm: $^4S_{3/2} \rightarrow {}^4I_{15/2}$. As compared to the $^4S_{3/2} \rightarrow {}^4I_{15/2}$ transition, the emission intensity of the $^2H_{11/2} \rightarrow {}^4I_{15/2}$ transition shows a monotonic increase with no evident shift in the position of the band with the increase of temperature, which indicates that the $^2H_{11/2}$ level can be effectively populated from the $^4S_{3/2}$ level through the thermal excitation process.[59] Furthermore, the increase of temperature is also advantageous for reducing the structural defects and surface ligands. Thus, the thermally coupled level (TCLs) method is assumed to be applicable for the optical thermometry. Based on the Boltzmann distribution law, the LIR of two TCL emissions ($^2H_{11/2}$ and $^4S_{3/2}$) can be written as eqn (3).[60–62]

$$\mathrm{LIR} = \frac{I_H}{I_S} = A\exp\left(\frac{-\Delta E}{k_b T}\right) \tag{3}$$

where I_H and I_S indicate the embedded intensities of the $^2H_{11/2} \rightarrow {}^4I_{15/2}$ (524–537 nm) and $^4S_{3/2} \rightarrow {}^4I_{15/2}$ (537–564 nm) transitions, respectively. A is a parameter that depends on the host lattice. ΔE is the energy gap between the levels $^2H_{11/2}$ and $^4S_{3/2}$, k_b and T are the Boltzmann constant (0.695 K^{-1} cm^{-1}), and the absolute temperature, respectively taking transforming eqn (3) to logarithmic format, eqn (4):

$$\ln(\mathrm{LIR}) = \ln(A) - \left(\frac{\Delta E}{k_b T}\right) \tag{4}$$

The absolute sensitivity S_a and the relative sensitivity S_r play very important roles in the determination of the practical application of the optical thermal sensing, which can be achieved by eqn (5) and (6).[63–65]

$$S_a = \left|\frac{\delta \mathrm{LIR}}{\delta T}\right| \tag{5}$$

$$S_r = \frac{1}{\mathrm{LIR}}\left|\frac{\delta \mathrm{LIR}}{\delta T}\right| \tag{6}$$

Besides the sensitivities, one also finds the temperature ambiguity (δT or ΔT). δT is the lowest measured variation of the temperature value during a given measurement, which is generally expressed as eqn (7):[66,67]

$$\delta T = \frac{1}{S_r} = \frac{\delta \mathrm{LIR}}{\mathrm{LIR}} \tag{7}$$

where δLIR is the uncertainty of the LIR parameter δLIR/LIR in our case is fixed at 0.5%.[68,69]

It is clear from Fig. 8(a) and (b) that the two intensity emission bands at 525 nm ($^2H_{11/2}$–$^4I_{15/2}$) and 552 nm ($^4S_{3/2}$–$^4I_{15/2}$) for both UC and DS are progressively attenuated with the increase in temperature. The potential for thermometry applications is related to the luminescence intensity ratio (LIR), which can be assessed using the eqn (3), Fig. 9(a) and (c) show plots of (LIR) *vs.* T for DS and UC respectively, while Fig. 9(b) and (d), plots ln LIR *vs.* the inverse temperature for DS and UC respectively, showing a linear behavior according to eqn (4). The slope values are $\Delta E/k_b = 797$ K for DS and $\Delta E/k_b = 789$ K for UC, respectively. Therefore, the $\Delta E/k_b$ parameter is not very sensitive to the change of the excitation source. The above discussions suggest that the $^2H_{11/2}$/$^4S_{3/2}$–$^4I_{15/2}$ transitions of the Er^{3+} ion can be used for radiometric temperature sensing with both 325 nm and 975 nm excitations. It is necessary to investigate the behavior of this pair of transitions over the two excitations. Marciniak *et al.* have confirmed that the relative sensitivity, (S_r), compared to the absolute sensitivity, (S_a), can be a witness of the critical performance of thermal sensors.[70] The absolute sensitivity (S_a) and the relative sensitivity (S_r) are described as absolute and relative change of the LIR value with respect to temperature variation, using eqn (5) and (6), respectively. Fig. 10(a) and (b) illustrate the corresponding optical thermometry sensitivities S_a and S_r for both UC and DS processes.

These results demonstrate that changes in excitation have a minor impact on sensitivities. Specifically, under 975 nm

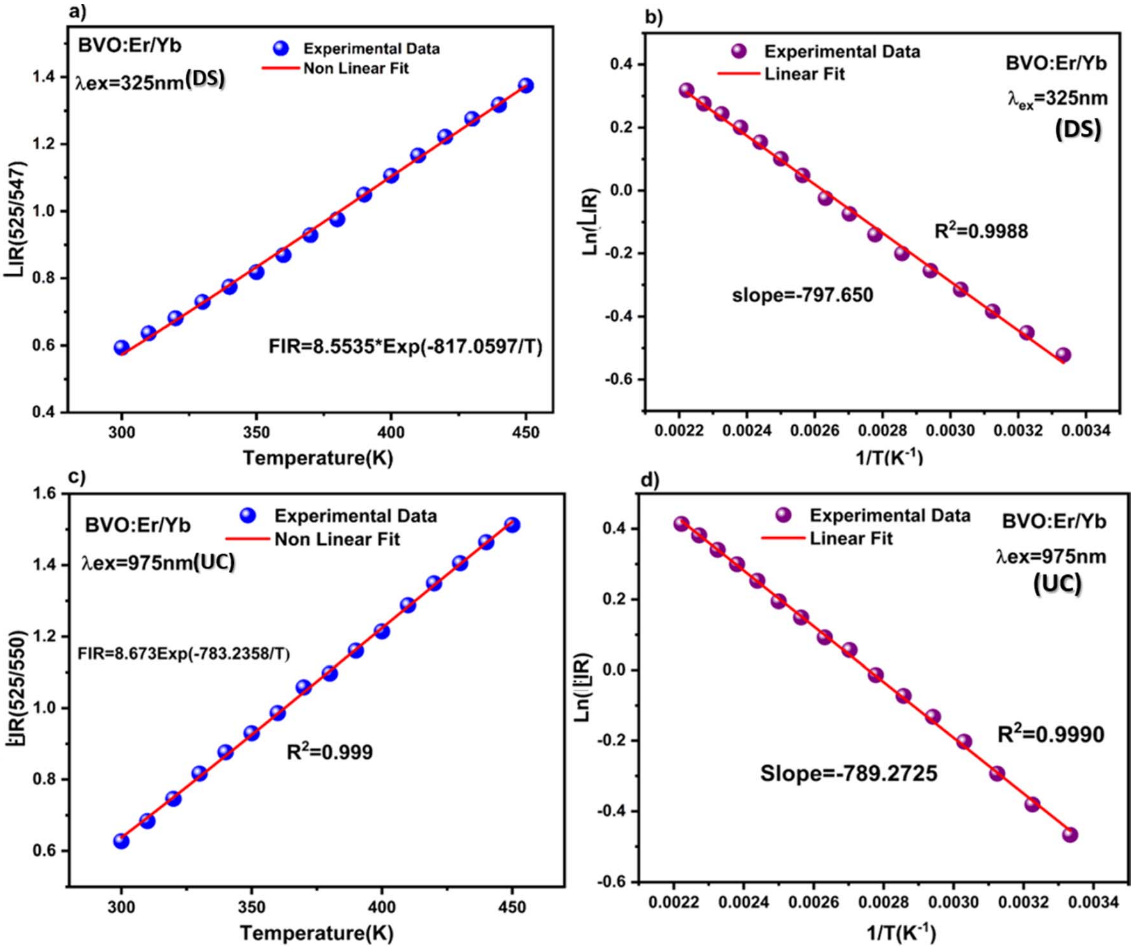

Fig. 9 Luminescence intensity ratio LIR as a function of temperature. (a) under 325 nm (DS); (c) under 975 nm (UC). Monolog plot of the LIR as a function of the inverse temperature(1/*T*). (b) under 325 nm (DS); (d) under 975 nm (UC).

excitation (UC), the maximum absolute sensitivity (S_a) reaches 60×10^{-4} K^{-1} at 388 K, whereas under 325 nm excitation (DS), (S_a) decreases to 56×10^{-4} K^{-1} at 400 K. However, the maximal relative sensitivity parameter, (S_r), is observed with the DS emission. Notably, for both excitations, (S_r) values consistently decrease with temperature from 300 K to 450 K, taking a value of

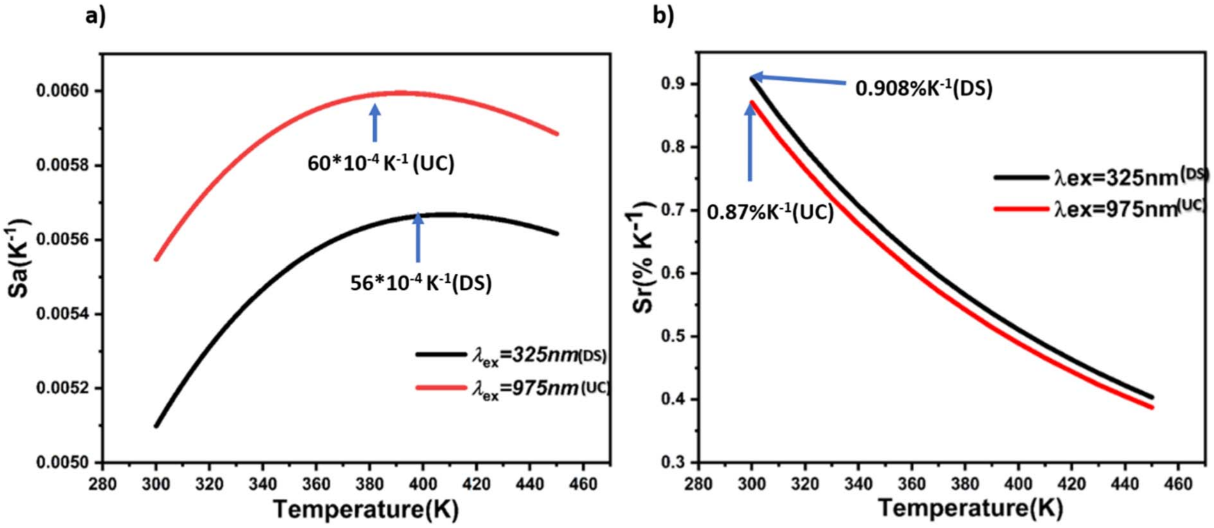

Fig. 10 (a) Absolute sensitivities (S_a) of BVO: Er/Yb phosphor as a function of temperature. (b) Relative (S_r) sensitivities of BVO: Er/Yb phosphor as a function of temperature.

Table 1 Sensitivities for the temperature-sensing luminescence materials

Sensing materials	T range (K)	λ_{exc} (nm)	$S_{a_{max}}$ (10^{-3} K)	$S_{r_{max}}$ (% K^{-1})	Ref.
LaNbO$_4$: Er/Yb	10–300	980	8.1 (430 K)	0.749 (300 K)	71
Ca$_3$(PO$_4$)$_2$: Er/Yb	300–473	980	—	0.34 (300 K)	72
LaPVO$_4$: Er/Yb	300–440	325	5.766 (360 K)	0.801 (300 K)	47
	300–520	980	4.38 (300 K)	0.7 (300 K)	
YPVO$_4$: Er/Yb	300–440	980	6.58 (100 K)	6.58 (100 K)	73
NaErF$_4$@NaYF$_4$@NaYbF$_4$: Tm@NaYF$_4$ NPs	293–413	980	—	0.71 (315 K)	74
GdPVO$_4$: Er/Yb	300–510	325	6.12 (380 K)	0.85 (300 K)	39
	300–440	980	5.07 (320 K)	0.63 (300 K)	
Silicate glass: Er/Yb	296–723	980	—	0.33 (296 K)	75
NaY (MoO$_4$)$_2$: Er/Yb	303–523	980	—	0.66 (373 K)	76
GdVO$_4$@SiO$_2$: Er/Yb	297–343	980	—	0.94 (343 K)	77
Y$_2$SiO$_5$: Er/Yb	—	975	—	0.7 (300 K)	78
La$_2$CaZnO$_5$: Er/Yb	303–573	980	—	0.71 (303 K)	79
BVO: Er/Yb	300–450K	325	5.6 (400 K)	0.908 (300 K)	This work
		975	6 (388 K)	0.87 (300 K)	

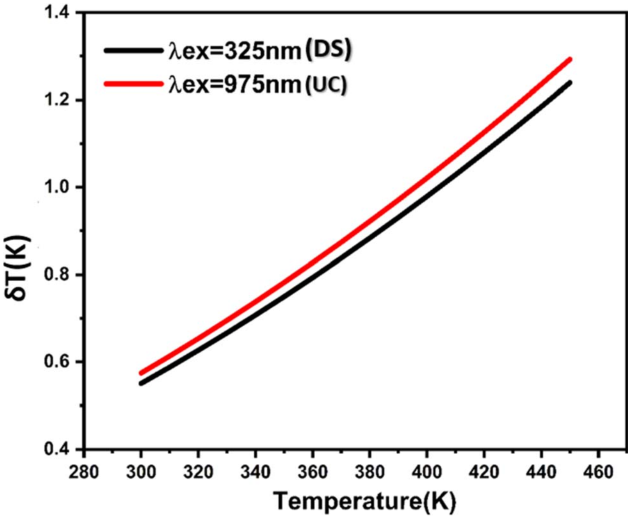

Fig. 11 Temperature (δT) resolution of BVO: Er/Yb phosphor as a function of temperature.

0.908% K^{-1} and 0.87% K^{-1} at 300 K for the DS and UC processes, respectively. Table 1 displays the optical temperature parameters of various luminescence materials. In comparison, the samples prepared in our study exhibit relatively high sensitivity across a wide temperature range, suggesting that the novel strategy employed here can be further explored to understand temperature-dependent dual-mode optical properties. The temperature resolution, as calculated using eqn (7), is depicted in Fig. 11. Under excitation at 325 nm, the temperature resolution δT gradually rises from 0.55 to 1.23 K as the temperature increases from 300 to 450 K. Conversely, the δT obtained under 975 nm excitation closely mirrors that found under excitation at 325 nm. This evidences that the excitation source does not influence the temperature resolution significantly, but the sensitivity achieved *via* the DS process. The BiVO$_4$ doped Er^{3+}/Yb^{3+} codoped phosphors could be potential candidates for optical thermometry applications.

6. Conclusion

In summary, we successfully synthesized pure and codoped Er^{3+}/Yb^{3+} doped bismuth vanadate using the sol–gel method, with their crystal structures confirmed *via* XRD analysis. BVO: Er/Yb exhibits notable up-conversion (UC) and down shifting (DS) emissions, making of it a promising dual-mode phosphor. We investigated the performance of these luminescent thermometers in terms of thermal sensitivities and temperature uncertainties under both UC and DS processes, employing the self-referenced luminescence intensity ratio technique. The thermal sensor was evaluated in the 300–450 K temperature range using the $^2H_{11/2} \rightarrow {}^4I_{15/2}$ and $^4S_{3/2} \rightarrow {}^4I_{15/2}$ transitions of Er^{3+} ions. We have demonstrated that changes in excitation have a minor impact on sensitivities. Specifically, under 975 nm excitation (UC), the maximum absolute sensitivity (S_a) reaches 60×10^{-4} K^{-1} at 388 K, whereas under 325 nm excitation (DS), (S_a) decreases to 56×10^{-4} K^{-1} at 400 K. However, the maximal relative sensitivity parameter, (S_r), is observed for the DS process. Notably, for both excitation processes, the S_r values consistently decrease with temperature in the range of 300 K to 450 K. They peak at 0.908% K^{-1}(DS) and 0.87% K^{-1}(UC) at 300 K, gradually declining to 0.4% K^{-1} (DS) and 0.39% K^{-1} (UC) at 450 K for the DS and UC processes, respectively. The temperature resolution gradually increases from 0.55 to 1.23 K with increasing temperature under 325 nm excitation. Interestingly, the resolution under 980 nm excitation closely resembles that under 325 nm excitation, indicating minimal influence of excitation source on temperature resolution. Our findings underscore the nearly identical nature of up conversion and downshifting processes in influencing the performance of thermometric sensors when BiVO$_4$ codoped with Er^{3+}/Yb^{3+}is utilized as the host material. This work not only advances our understanding of luminescent thermometry but also holds promise for diverse applications in environmental monitoring and materials science.

Data availability

All data underlying the results are available as part of the article and no additional source data are required.

Conflicts of interest

There are no conflicts to declare.

Acknowledgements

Fadwa Ayacha received partial funding through the Erasmus+ KA171 Project. I. Mediavilla and J. Jimenez were partially funded by the Spanish Ministry of Science and Innovation (Grants PID2021-126046OB-C22, PID2020-113533RB-C33, TED2021-130786B-I00) and the Regional Government of Castilla y León (Junta de Castilla y León). Additional funding was provided by the Ministry of Science and Innovation and the European Union's NextGeneration EU/PRTR under the project "Programa Complementario de Materiales Avanzados".

References

1 B. Zhuang, Y. Liu, S. Yuan, H. Huang, J. Chen and D. Chen, *Nanoscale*, 2019, **11**, 15010–15016.
2 Y. Gao, F. Huang, H. Lin, J. Zhou, J. Xu and Y. Wang, *Adv. Funct. Mater.*, 2016, **26**, 3139–3145.
3 B. Dong, B. Cao, Y. He, Z. Liu, Z. Li and Z. Feng, *Adv. Mater.*, 2012, **15**, 1987–1993.
4 C. D. S. Brites, S. Balabhadra and L. D. Carlos, *Adv. Opt. Mater.*, 2019, **7**, 1801239.
5 X. Qiu, Q. Zhou, X. Zhu, Z. Wu, W. Feng and F. Li, *Nat. Commun.*, 2020, **11**, 4.
6 Z. Zhang, H. Suo, X. Zhao and C. Guo, *Photonics Res.*, 2020, **8**, 32–38.
7 M. Sekulić, V. Đorđević, Z. Ristić, M. Medić and M. D. Dramićanin, *Adv. Opt. Mater.*, 2018, **6**, 1800552.
8 Y. Pan, X. Xie, Q. Huang, C. Gao, Y. Wang, L. Wang, B. Yang, H. Su, L. Huang and W. Huang, *Adv. Mater.*, 2018, **30**, 1705256.
9 X. Chen, S. Liu, K. Huang, J. Nie, R. Kang, X. Tian, S. Zhang, Y. Li and J. Qiu, *Chem. Eng. J.*, 2020, **396**, 125201.
10 Y. Gao, Y. Cheng, T. Hu, Z. Ji, H. Lin, J. Xu and Y. Wang, *J. Mater. Chem. C*, 2018, **6**, 11178–11183.
11 Z. Zheng, J. Zhang, X. Liu, R. Wei, F. Hu and H. Guo, *Ceram. Int.*, 2020, **46**, 6154–6159.
12 H. Zhang, H. Yang, G. Li, S. Liu, H. Li, Y. Gong, Y. Liang and Y. Chen, *Chem. Eng. J.*, 2020, **396**, 125251.
13 X. Zhang, Z. Zhu, Z. Guo, Z. Sun and Y. Chen, *Chem. Eng. J.*, 2019, **356**, 413–422.
14 L. Li, X. Tang, Z. Wu, Y. Zheng, S. Jiang, X. Tang, G. Xiang and X. Zhou, *J. Alloys Compd.*, 2019, **780**, 266–275.
15 Y. Jiang, Y. Tong, S. Chen, W. Zhang, F. Hu, R. Wei and H. Guo, *Chem. Eng. J.*, 2021, **413**, 127470.
16 M. D. Dramićanin, *J. Appl. Phys.*, 2020, **128**, 040902.
17 M. Lin, L. Xie, Z. Wang, B. S. Richards, G. Gao and J. Zhong, *J. Mater. Chem. C*, 2019, **7**, 2971–2977.
18 S. Wang, H. Zhou, X. Wang and A. Pan, *J. Phys. Chem. Solids*, 2016, **98**, 28–31.
19 K. Green, K. Huang, H. Pan, G. Han and S. F. Lim, *Front. Chem.*, 2018, **6**, 416.
20 X. Wang, Y. Wang, J. Yu, Y. Bu and X. Yan, *Opt. Express*, 2018, **26**, 21950.
21 M. Ding, Z. Shen, Y. Yuan, W. Bai, C. Lu and Z. Ji, *Ceram. Int.*, 2018, **44**, 14884–14890.
22 F. Ayachi, K. Saidi, M. Dammak, W. Chaabani, I. Mediavilla-Martínez and J. Jiménez, *Mater. Today Chem.*, 2023, **27**, 101352.
23 F. Ayachi, K. Saidi, K. Soler-Carracedo, M. Dammak and I. R. Martín, *J. Alloys Compd.*, 2023, **961**, 171146.
24 S. F. León-Luis, U. R. Rodríguez-Mendoza, E. Lalla and V. Lavín, *Sens. Actuators, B*, 2011, **158**, 208–213.
25 D. Wawrzynczyk, A. Bednarkiewicz, M. Nyk, W. Strek and M. Samoc, *Nanoscale*, 2012, **4**, 6959.
26 A. Pandey, S. Som, V. Kumar, V. Kumar, K. Kumar, V. K. Rai and H. C. Swart, *Sens. Actuators, B*, 2014, **202**, 1305–1312.
27 W. A. Pisarski, J. Pisarska, R. Lisiecki and W. Ryba-Romanowski, *Opt. Mater.*, 2016, **59**, 87–90.
28 D. Manzani, J. F. D. S. Petruci, K. Nigoghossian, A. A. Cardoso and S. J. Ribeiro, *Sci. Rep.*, 2017, **7**, 1–11.
29 K. Zhou, H. Zhang, Y. Liu, Y. Bu, X. Wang and X. Yan, *J. Am. Ceram. Soc.*, 2019, **102**, 6564–6574.
30 J. Cao, D. Xu, F. Hu, X. Li, W. Chen, L. Chen and H. Guo, *J. Eur. Ceram. Soc.*, 2018, **38**, 2753–2758.
31 R. L. Frost, D. A. Henry, M. L. Weier and W. Martens, *J. Raman Spectrosc.*, 2006, **37**, 722–732.
32 C. Regmi, Y. K. Kshetri, S. H. Jeong and S. W. Lee, *J. Appl. Phys.*, 2019, **125**, 043101.
33 K. V. Terebilenko, K. L. Bychkov, V. N. Baumer, N. S. Slobodyanik, M. V. Pavliuk, A. Thapper, I. I. Tokmenko, I. M. Nasieka and V. V. Strelchuk, *Dalton Trans.*, 2016, **45**, 3895–3904.
34 L. Shan and Y. Liu, *J. Mol. Catal. Chem.*, 2016, **416**, 1–9.
35 W. Zheng, P. Huang, D. Tu, E. Ma, H. Zhu and X. Chen, *Chem. Soc. Rev.*, 2015, **44**, 1379–1415.
36 F. Wang, D. Banerjee, Y. Liu, X. Chen and X. Liu, *Analyst*, 2010, **135**, 1839–1854.
37 Y. Liu, L. Meng, H. Wang, J. Jiao, M. Xing, Y. Peng, X. Luo and Y. Tian, *Dalton Trans.*, 2021, **50**, 960–969.
38 J. Sun, Z. Zhang, H. Suo, Y. Chen, J. Xiang and C. Guo, *Ceram. Int.*, 2021, **47**, 409–415.
39 Y. K. Kshetri, C. Regmi, B. Chaudhary, H.-S. Kim, T.-H. Kim, F. Rosei and S. W. Lee, *J. Lumin.*, 2021, **230**, 117739.
40 S. Lotfi, A. Assani, M. Saadi and H. A. Ahsaine, *Mater. Today Proc.*, 2022, **61**, 487–497.
41 C. Li, B. Dong, S. Li and C. Song, *Chem. Phys. Lett.*, 2007, **443**, 426–429.
42 M. Azdouz, B. Manoun, M. Azrour, L. Bih, L. El Ammari, S. Benmokhtar and P. Lazor, *J. Mol. Struct.*, 2010, **963**, 258–266.
43 U. Opara Krašovec, B. Orel, A. Šurca, N. Bukovec and R. Reisfeld, *Solid State Ionics*, 1999, **118**, 195–214.
44 R. T. Harley, W. Hayes and S. R. P. Smith, *Solid State Commun.*, 1971, **9**, 515–517.

45 A. Dwivedi, E. Rai, D. Kumar and S. B. Rai, *ACS Omega*, 2019, **4**, 6903–6913.

46 K. Saidi, C. Hernández-Álvarez, M. Runowski, M. Dammak and I. Rafael Martín Benenzuela, *ACS Appl. Nano Mater.*, 2023, **6**, 19431–19442.

47 F. Ayachi, K. Saidi, M. Dammak, W. Chaabani, I. Mediavilla-Martínez and J. Jiménez, *Mater. Today Chem.*, 2023, **27**, 101352.

48 F. H. Borges, J. C. Martins, F. J. Caixeta, R. R. Pereira, L. D. Carlos, R. A. S. Ferreira and R. R. Gonçalves, *J. Sol-Gel Sci. Technol.*, 2022, **102**, 249–263.

49 P. Woźny, K. Soler-Carracedo, M. Perzanowski, J. Moszczyński, S. Lis and M. Runowski, *J. Mater. Chem. C*, 2024, **12**, 11824–11835.

50 A. Dwivedi, K. Mishra and S. B. Rai, *J. Phys. Appl. Phys.*, 2015, **48**, 435103.

51 N. M. Bhiri, M. Dammak, J. J. Carvajal, M. Aguiló, F. Díaz and M. C. Pujol, *J. Alloys Compd.*, 2022, **921**, 166020.

52 I. Kchaou, K. Saidi, R. Salhi and M. Dammak, *RSC Adv.*, 2022, **12**, 7529–7539.

53 K. Saidi and M. Dammak, *RSC Adv.*, 2020, **10**, 21867–21875.

54 H. Dong, L.-D. Sun and C.-H. Yan, *Chem. Soc. Rev.*, 2015, **44**, 1608–1634.

55 M. Pollnau, D. R. Gamelin, S. R. Lüthi, H. U. Güdel and M. P. Hehlen, *Phys. Rev. B:Condens. Matter Mater. Phys.*, 2000, **61**, 3337–3346.

56 J. F. Suyver, A. Aebischer, S. García-Revilla, P. Gerner and H. U. Güdel, *Phys. Rev. B:Condens. Matter Mater. Phys.*, 2005, **71**, 125123.

57 H. Cui, Y. Cao, Y. Zhang, L. Cao, S. Ran, X. Wang, D. Wu, X. Li, X. Zhang and B. Chen, *J. Lumin.*, 2022, **241**, 118484.

58 Y. Chen, Y. Bu, X. Chen, Y. Zhang, Y. Shen, L. Zhou and D. Deng, *J. Lumin.*, 2022, **250**, 119121.

59 W. Xu, Y. Cui, Y. Hu, L. Zheng, Z. Zhang and W. Cao, *J. Alloys Compd.*, 2017, **726**, 547–555.

60 C. Hernández-Álvarez, P. I. Martín-Hernández, I. R. Martín, F. Rivera-López, H. Hemmerich, J. Llanos and M. Runowski, *Appl. Mater. Today*, 2024, **38**, 102207.

61 H. Cui, Y. Cao, Y. Zhang, T. Peng, L. Cao, S. Ran, Y. Wang, D. Wu, X. Li, X. Zhang and B. Chen, *Ceram. Int.*, 2021, **47**, 21271–21275.

62 I. Kachou, K. Saidi, C. Hernández-Álvarez, M. Dammak and I. R. Martín, *Adv. Mater.*, 2024, **5**, 8280–8293.

63 K. Saidi, M. Yangui, C. Hernández-Álvarez, M. Dammak, I. Rafael Martín Benenzuela and M. Runowski, *ACS Appl. Mater. Interfaces*, 2024, **16**, 19137–19149.

64 M. Yangui, K. Saidi, C. Hernández-Álvarez, M. Dammak and I. R. Martín, *J. Alloys Compd.*, 2025, **1010**, 177958.

65 F. Ayachi, K. Saidi, W. Chaabani and M. Dammak, *J. Lumin.*, 2021, **240**, 118451.

66 F. Ayachi, K. Saidi, M. Dammak, J. J. Carvajal and M. C. Pujol, *RSC Adv.*, 2024, **14**, 13494–13504.

67 F. Ayachi, K. Saidi and M. Dammak, *Adv. Mater.*, 2024, **5**, 6162–6169.

68 O. A. Savchuk, J. J. Carvajal, C. D. S. Brites, L. D. Carlos, M. Aguilo and F. Diaz, *Nanoscale*, 2018, **10**, 6602–6610.

69 F. Ayachi, K. Saidi, M. Dammak, J. Josep Carvajal and M. Cinta Pujol, *RSC Adv.*, 2024, **14**, 13494–13504.

70 L. Marciniak, A. Bednarkiewicz, D. Hreniak and W. Strek, *J. Mater. Chem. C*, 2016, **4**, 4327–4328.

71 K. Pavani, J. P. C. do Nascimento, S. K. Jakka, F. F. do Carmo, A. J. M. Sales, M. J. Soares, M. P. F. Graça, F. J. A. de Aquino, D. X. Gouveia and A. S. B. Sombra, *J. Lumin.*, 2021, **235**, 117992.

72 K. M. Krishna, S. P. Tiwari, A. Kumar and K. Kumar, *Sens. Actuators, A*, 2020, **315**, 112302.

73 F. Ayachi, K. Saidi, W. Chaabani and M. Dammak, *J. Lumin.*, 2021, **240**, 118451.

74 L. Lei, X. Dai, Y. Cheng, Y. Wang, Z. Xiao and S. Xu, *J. Mater. Chem. C*, 2019, **7**, 3342–3350.

75 C. Li, B. Dong, S. Li and C. Song, *Chem. Phys. Lett.*, 2007, **443**, 426–429.

76 X. Yang, Z. Fu, Y. Yang, C. Zhang, Z. Wu and T. Sheng, *J. Am. Ceram. Soc.*, 2015, **98**, 2595–2600.

77 O. A. Savchuk, J. J. Carvajal, C. Cascales, M. Aguiló and F. Díaz, *ACS Appl. Mater. Interfaces*, 2016, **8**, 7266–7273.

78 N. Rakov and G. S. Maciel, *Sens. Actuators, B*, 2012, **164**, 96–100.

79 V. Kumar, S. Som, S. Dutta, S. Das and H. C. Swart, *RSC Adv.*, 2016, **6**, 84914–84925.